Proceedings of the ASME 2010 3rd Joint US-European Fluids Engineering Summer Meeting and 8th International Conference on Nanochannels, Microchannels, and Minichannels
FEDSM-ICNMM2010
August 1-5, 2010, Montreal, Canada

FEDSM-ICNMM2010-30387

THE LOW REYNOLDS NUMBER LIMIT OF VORTEX AND WAKE-INDUCED VIBRATIONS

Stéphane Étienne*
Researcher
Département de Génie Mécanique
École Polytechnique de Montréal
C.P. 6079, Succ. centre-ville
Montréal (Québec)
H3C 3A7, Canada
stephane.etienne@polymtl.ca

Dominique Pelletier
Canada Research Chair
Département de Génie Mécanique
École Polytechnique de Montréal
C.P. 6079, Succ. centre-ville
Montréal (Québec)
H3C 3A7, Canada
dominique.pelletier@polymtl.ca

ABSTRACT

Vortex and wake induced vibrations (VIV/WIV) of a circular cylinder at low values of the Reynolds number (Re) are simulated by means of a fully coupled fluid-structure interaction numerical model based on the finite element method. It is shown that VIV/WIV could occur far below the first Hopf bifurcation (Re <47). The main objective of this study is to determine the limiting Reynolds-Reduced velocity (Ur) curve that separates the non-vibrational area from the possible vibrations occurrence area. We assume that by taking a zero mass cylinder and zero structural damping we will obtain the low limit of vibrations in terms of Re and Ur. It is shown in particular that transverse vibrations could occur for reduced velocities larger than 40 and not below 3.5.

NOMENCLATURE

D Cylinder diameter.
U Free-stream velocity.
k Spring rigidity.
ζ Damping ratio.
m Unit length cylinder mass.
ρ_f Fluid density.
μ Fluid dynamic viscosity.
ρ_c Cylinder density.
ρ_c Reynolds number.
$Re = \rho_f UD/\mu$ mass ratio.
$Cd = 2f_x/(\rho_f U^2 D)$ Drag coefficient.
$Cl = 2f_y/(\rho_f U^2 D)$ Lift coefficient.
$m_a = \rho_f \pi D^2/4$ Fluid added mass.
$\mathbf{x} = [x,y]^t$ Cylinder vector displacement.
$\mathbf{x}^* = \mathbf{x}/D$ Non-dimensionnalized cylinder vector displacement.
$Ur^* = 2\pi U/(\sqrt{k/mD})$ Reduced velocity in air.
$Ur = 2\pi U/(\sqrt{k/(m+m_a)}D)$ Reduced velocity in water.
f^* Effective reduced vibration frequency.
$f_{Nw} = 1/Ur$ Cylinder reduced frequency in water.

1 Introduction

The flow behind a stationary circular cylinder becomes unstable when the Reynolds number (Re) is higher than a critical value Re_c of approximately 47 called the first Hopf bifurcation. Vortices are shed from the cylinder resulting in the appearance of a Von Karman vortex street. No vortex is shedded for Reynolds numbers below 47. A priori, there is no evident reason for the occurrence of vortex-induced vibrations (VIV) below this critical value. However, for Reynolds number value higher than approxi-

*Address all correspondence to this author.

mately 30 and less than 47 the wake exhibits asymmetries. Thus, one may wonder what would happen if the cylinder is mounted on springs and allowed to move in response to the flow loads for values of *Re* lower than 47. This study is motivated by vibration problems that could occur in small scale systems such as hot-wire probes (*e.g.*, see Van Atta and Gharib [1]).

Cossu and Morino [2] stressed that for mass ratios higher than 7, vortex-induced vibrations occur at a Reynolds number as low as 23.5. In Mittal and Singh [3], vortex-induced vibrations at subcritical Reynolds ($Re < Re_c$) have been studied. Selected cases were studied for mass ratios of 4.73 and higher and reduced velocities ranging from 5 to 11. They found that vortex-induced vibrations occur at a Reynolds number as low as 20. In fact no vibrations are obtained at 20 but a maximum vibration amplitude of 0.17 is obtained at *Re*=21. Thus, it appears that vibrations are likely to happen for low Reynolds number values.

In the objective to determine the limiting Reynolds-Reduced velocity curve that separates the non-vibrational area from the possible vibrations occurrence area, we propose to perform simulations for a mass ratio equal to zero - the cylinder possesses no mass - and no structural damping. It seems natural to introduce zero external damping in this problem. However, it is not trivial to think that the lowest possible cylinder mass will favor the occurrence of vibrations. From Mittal and Singh [3] we learned that increasing the mass ratio decreases the reduced velocity range of VIV for a given Reynolds number. This is in accordance with several other results (see *e.g.* Stappenbelt and Lalji [4], Shiels *et al.* [5]). Moreover, for a given reduced velocity, VIV will occur at a higher Reynolds number. Mass ratios higher than 4.73 were considered in Mittal and Singh [3].

Here, we show the result of a parametric study with respect to the reduced velocity $Ur = U/(f_c D)$ and Reynolds number $Re = UD/\nu$, with U the uniform flow velocity, f_c the natural frequency of the cylinder in still water [$f_c = \sqrt{k/(m_c+m_a)}/(2\pi)$] and D its diameter. k is the rigidity of the spring that supports a unit length cylinder, m_c is its mass per unit length and the added mass due to the surrounding water is $m_a = \rho_f \pi D^2/4$. For zero mass cylinders, the mass ratio defined as $m^* = \rho_c/\rho_f$ is also null. This results in $f_c = \sqrt{k/m_a}/(2\pi)$. Thus, the reduced velocity in water of a massless circular cylinder is $Ur = \pi U\sqrt{\rho_f \pi/k}$.

We begin with the equations modeling this fluid-structure interaction problem. Then, the numerical model used will briefly be described. Finally, after validation tests, results for various values of the Reynolds number and reduced velocities will be shown.

2 Numerical Method

In this section, we describe the numerical method that has been used for all the computations presented herein.

2.1 Governing Equations

The flow of an incompressible fluid, in an arbitrary time-dependent coordinate system is described by the continuity and momentum equations [6] written as

$$\nabla \cdot \mathbf{u} = 0 \tag{1}$$

$$\rho_f \mathbf{u}_{,t} + \rho_f[(\mathbf{u}-\mathbf{v})\cdot\nabla]\mathbf{u} = \nabla\cdot\boldsymbol{\sigma} \tag{2}$$

where $\mathbf{v}$ is the velocity of the moving reference frame, ρ_f the fluid density, $\mathbf{u}$ the fluid velocity, $\boldsymbol{\sigma}$ the total fluid stress tensor (pressure and viscous forces). Eq. (1) and (2) are expressed in an Arbitrary Lagrangian Eulerian (ALE) coordinate system. Details of its development may be found in [7]. Assuming that the fluid is Newtonian, its constitutive equation is given by

$$\boldsymbol{\sigma} = \boldsymbol{\tau} - p\mathbf{I} \text{ with } \boldsymbol{\tau} = \mu[\nabla\mathbf{u} + (\nabla\mathbf{u})^T]$$

where μ is the dynamic viscosity and p is the fluid pressure. The flow equations are closed with the following boundary conditions,

$$\begin{aligned} \boldsymbol{\sigma}\cdot\mathbf{n} &= \bar{\mathbf{t}} \text{ on } \Gamma_N \\ \mathbf{u} &= \bar{\mathbf{u}} \text{ on } \Gamma_D \end{aligned} \tag{3}$$

where Γ_N denotes a boundary on which Neumann conditions are applied in the form of prescribed surface forces (tractions) $\bar{\mathbf{t}}$, and Γ_D corresponds to a Dirichlet boundary on which the velocity, $\bar{\mathbf{u}}$, is imposed.

The cylinder is supported by constant rigidity springs without mass and dampers. Time is non dimensionalized as $t = Ut^*/D$. Its equations of motions cylinder are

$$\left(\frac{2\pi}{Ur}\right)^2 \mathbf{x}^* = \frac{2}{\pi}[Cd, Cl]^t \tag{4}$$

with $\mathbf{x}^* = [x/D, y/D]^t$ the non-dimensional cylinder vector displacement and $[Cd, Cl]^t$ the non-dimensional force coefficients (Drag and Lift) in x and y directions. These force coefficients are written as functions of f_x and f_y the fluid loading for each direction as follows

$$Cd = \frac{f_x}{\frac{1}{2}\rho_f D U^2} \tag{5}$$

$$Cl = \frac{f_y}{\frac{1}{2}\rho_f D U^2} \tag{6}$$

There remains the issue of how to generate and control the grid motion and mesh velocities, *i.e.* manage the domain deformation. This can be done in several ways which only affect the ability of the solver to cope with more or less complicated domain deformations and mesh motions [8, 9]. We have opted to implement mesh control with the pseudo-solid approach of Sackinger [9] because it allows for a fully coupled continuum formulation. The pseudo-solid model provides physics-based rules using elasticity equations to describe the deformation of the time-varying domain.

2.2 Solution Strategy

We use a monolithic solution strategy coupling all degrees of freedom. The degrees of freedom in the fluid domain are the velocity vector, the pressure and the pseudo-solid displacements. They are fully coupled to the cylinder point mass displacements and velocities. In this approach all equations are treated implicitly in the time integration scheme and thus solved simultaneously. We use the 3^{rd} order Radau IIA implicit Runge-Kutta (IRK) scheme which is temporally 3^{rd} order accurate for velocity and 2^{nd} order accurate for the pressure (see Hairer *et al.* [10]).

This methodology is applicable not only for flows on deforming meshes but also to fully implicit monolithic treatment of unsteady Fluid-Structure Interactions. Linearisation of the flow and mesh equations must account for all implicit dependencies to ensure quadratic convergence of Newton's method. These steps are implemented simply and in a straight forward manner through the use of numerical Jacobians. This approach is very robust and applicable to a broad spectrum of problems.

The fluid velocity and displacement fields are discretized using 6-noded quadratic elements. Fluid pressure is discretized by piecewise linear continuous functions. The resulting sparse matrix system is solved using the PARDISO software [11, 12]. Details of the finite element flow solver and its verification with respect to time order accuracy and geometric conservation law on deforming domains can be found in Etienne *et al.* [13].

3 Validation and numerical details

Validation of computations is performed in two steps. A grid size and time step convergence study is performed. Then, predictions are compared with available results in the literature for configurations close to those studied here. All the cases treated here have one same set of boundary conditions. Dirichlet BC at the inflow boundary, Symmetry conditions at the top and lower boundaries and Neumann-free conditions at the outflow boundary. No-slip is applied on the cylinder. These conditions as well as the geometry are illustrated on Fig. 1

3.1 Convergence study

Briefly, a convergence study has been conducted showing that a non-dimensional time-step $U\Delta t/D = 0.1$ and a grid size made of 30K P2-P1 nodes is sufficient to ensure an accuracy of at least 3 significant digits of the Drag and Lift coefficients.

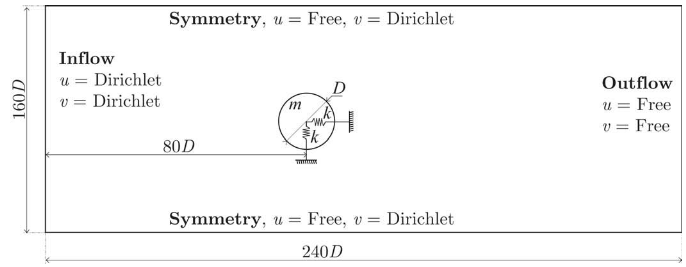

FIGURE 1. Geometry and boundary conditions.

We made comparisons with a 60K P2-P1 grid and a time-step of $U\Delta t/D = 0.02$. This tells us that sufficient accuracy is obtained with selected parameters. Note that third order time accuracy allows us to take a large time-step compared to lower order time integrators at the cost of a double-sized matrix. The grid used for computations is shown on Fig. 2 and 3.

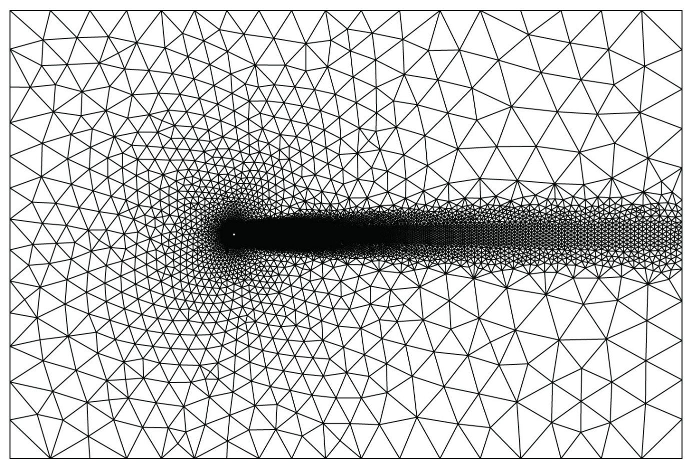

FIGURE 2. Computational grid used for all computations.

3.2 Validation tests

With the parameters described in section 3.1, we show two well documented comparison tests. The first one is that of a fixed circular cylinder in cross-flow at *Re*=200 while the second is a classical validation test for VIV.

For the case of a single fixed cylinder in cross flow, Table 1 compares results from different references (all numerical references) with those obtained with the present formulation. The drag and lift coefficients and the Strouhal number have been obtained by analysis over a time length of 20 vortex sheddings periods. The drag coefficient is the mean value of the in-line non-dimensioned force and the lift coefficient is computed as the root

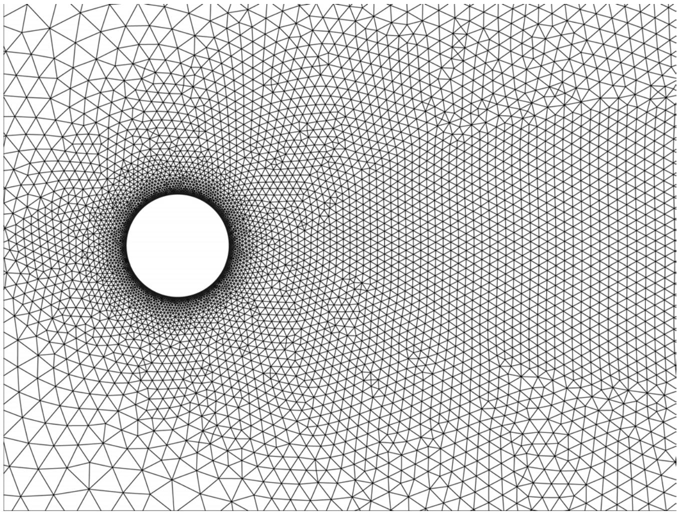

FIGURE 3. Close-up view of the computational grid at cylinder proximity.

mean square of the non-dimensionalized transverse load. The transient phase corresponding to the 50 first non-dimensional time units has been discarded. Our results are in good agreement with those obtained in the literature. However, while the Strouhal number is well captured, lot of scatter can be observed with regards to the lift coefficients among the numerical results collected here. The value we computed is close to the average of the previously computed values.

TABLE 1. Fixed cylinder at $Re = 200$.

Fixed single cylinder	$\bar{C}_d$	$C_{l\,rms}$	St
Halse [14] (1997)	1.35	0.62	0.196
Sa& Chang [15] (1991)	1.13	0.34	0.186
Braza [16] (1981)	1.38	0.76	0.190
Present Results	1.36	0.67	0.195

We now turn our attention on the second validation case that exercises the whole computational methodology. We have chosen the documented case of an isolated cylinder in cross flow. The cylinder is supported by constant rigidity springs and dampers in both directions. For this case, we rewrite the equations of motion of the cylinder taking into account that both its mass and structural damping are non-zero. We will use the mass ratio $m^* = \rho_c/\rho_f$ to non-dimensionalize the equations of motion of the cylinder. We get

$$\ddot{\mathbf{x}}^* + 2\zeta\left(\frac{2\pi}{Ur^*}\right)\dot{\mathbf{x}}^* + \left(\frac{2\pi}{Ur^*}\right)^2 \mathbf{x}^* = \frac{2}{\pi m^*}[Cd, Cl]^t \qquad (7)$$

with $\mathbf{x}^* = [x^*, y^*]^t = \mathbf{x}/D$ the vector of displacements in x and y, f_x and f_y the fluid loading in each direction. For this case, we compare with numerical results reported by Blackburn *et al.* (2000) [17] and Yang *et al.* (2008) [18]. In both studies as well as in the present validation case, the Reynolds number value is set to 200, the damping ratio ζ is equal to 0.01, the reduced velocity $Ur^* = U/(f_{air}D) = 2\pi U/(\sqrt{k/mD})$ is equal to 5 and the mass ratio m^* is equal to $4/\pi$. Fig. 4 shows the periodical trajectory

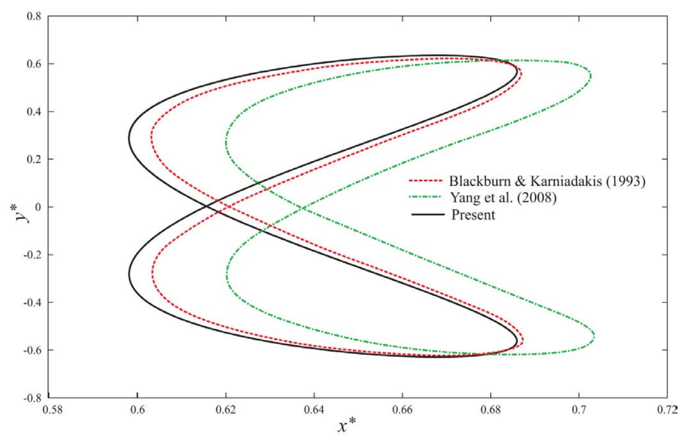

FIGURE 4. Trajectory of an isolated cylinder in cross-flow at Ur^*=5 and Re=200.

of the cylinder. Note that the horizontal and vertical scales differ $x^* \in [0.58, 0, 72]$, $y^* \in [-0.8, 0.8]$. The small range in x explains why disparity between the three results is magnified in the in-line direction. However, there is small discrepancy between them. Yang *et al.* (2008) [17] results are 3% downstream in terms of the center of the eight type trajectory compared to Blackburn *et al.* (2000) [18] and present results. In the present computations, we have verified that results are converged in terms of time step and space discretization.

These validation tests show that results obtained with the finite element code and selected time steps and grid size are reliable. In particular, VIV validation results were performed at a much higher Reynolds number than those presented hereafter. This comforts us in our choice of parameters.

4 Results

Computations have been performed for Reynolds number values below 47. As our aim is to get vibrational results of the cylinder, we accelerate the process by perturbing the flow at the beginning of the simulation. The inflow velocity is defined as follows

$$u = \cos(\pi(sin(2\pi t/T)) \quad (8)$$
$$v = \sin(\pi(sin(2\pi t/T)) \quad (9)$$

for $t \in [0,T]$ and

$$u = 1 \quad (10)$$
$$v = 0 \quad (11)$$

for $t \geq T$. We chose the non-dimensionalized period $T = 8.5$. The reason for such a choice comes from the Strouhal number value of 0.12 of the flow around a steady circular cylinder at $Re \sim 50$. We set $T = 1/St = 1/0.12 = 8.33 \sim 8.5$.

The perturbation at the initial stage of the simulation forces vortex-shedding and initiate vibrations. Oscillations will fade out if vibrations are not likely to occur. We consider to be in such a situation when the vibration amplitude becomes lower than $0.01D$. We observe that for a given reduced velocity, the amplitude of vibration decreases rapidly to zero as the Reynolds number is decreased. Thus, we expect no vibration for Reynolds number values below those giving a maximum transverse amplitude of $0.01D$.

The simulation time for all cases varies between 500 and 2000 non-dimensionalized time units. For cases with fast convergence toward a vibrational periodic result, simulations were stopped at 500. For near to the limit and non-vibration cases, simulation time was extended to 2000. We have performed around 50 simulations trying to encompass the vibrational frontier.

4.1 Frequencies

Fig. 5 shows the evolution of cylinder vibration frequencies times the reduced velocity as a function of the reduced velocity for all cases performed. For values of the reduced velocity below 3.5, no vibration occurred up to $Re = Re_c = 47$. But, for values higher, vibrations occurred for values beyond a certain Re value itself below Re_c. We can see on Fig. 5 that the reduced frequency does not depend on the cylinder frequency. It appears then that no lock-in is evidenced from this figure. This result is in accordance with those obtained by Shiels *et al.* [5] at $m^* = 0$ and $Re = 100$.

Fig. 6 shows the non-dimensional cylinder effective vibration frequency as a function of the reduced velocity. Even if the number of simulations treated should be increased, we observe

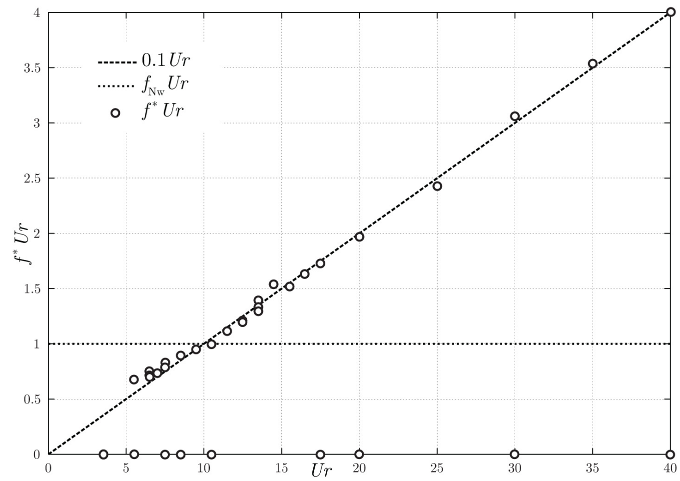

FIGURE 5. Cylinder vibration frequency times reduced velocity as a function of reduced velocity.

that when Ur is decreased for $Ur < 10$, f^* tends to increase. for $Ur > 10$, f^* increases slowly. All values are near to 0.1 and vary between 0.095 and 0.12. This is not so far from the Strouhal value at $Re = 50$. These results are in agreement with those obtained by Buffoni [19] who obtained Strouhal values experimentally for Reynolds numbers in the range $[20,50]$ by triggering vibrations of a cylinder. Our results allow to shed light on Buffoni's results.

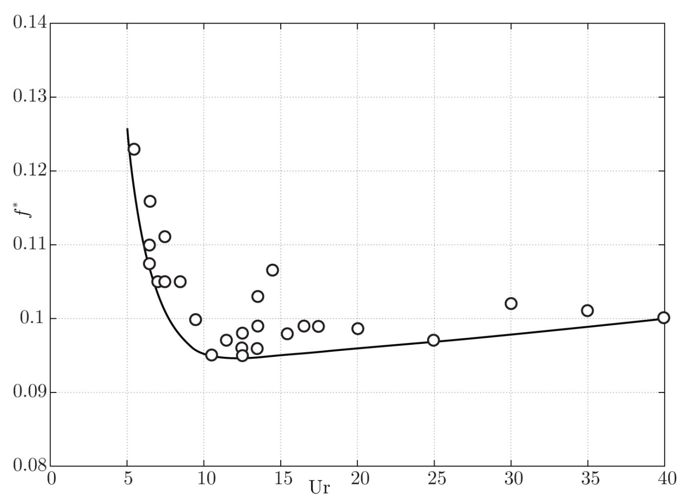

FIGURE 6. Non-dimensionnal cylinder effective vibration frequency.

4.2 Limit of vibrations

Fig. 7 shows the rough identification of the Reynolds number limit as a function of the reduced velocity beyond which vibrations of the cylinder occur. A finer resolution may be obtained by performing new computations around the limit. However, it seems clear from Fig. 7 that vibrations occur even for reduced velocities as high as 40 at a Reynolds number of 30. This is far below the critical Reynolds number value of 47.

We have also indicated on Fig. 7 for each vibrational case the maximum amplitude of vibration. We observe that, for a given Reynolds number, the amplitude tends to decrease with Ur for $Ur > 10$. For a given reduced velocity, amplitude increases with the Reynolds number.

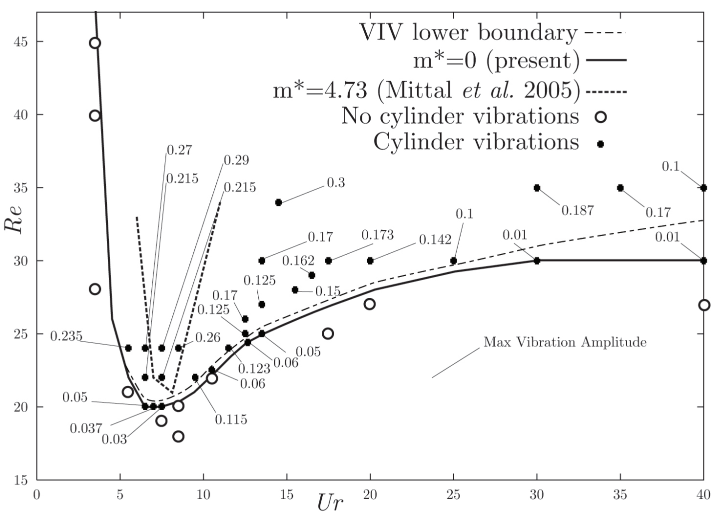

FIGURE 7. Vibrational frontier for $m^* = 0$ in the (Re, Ur) plane.

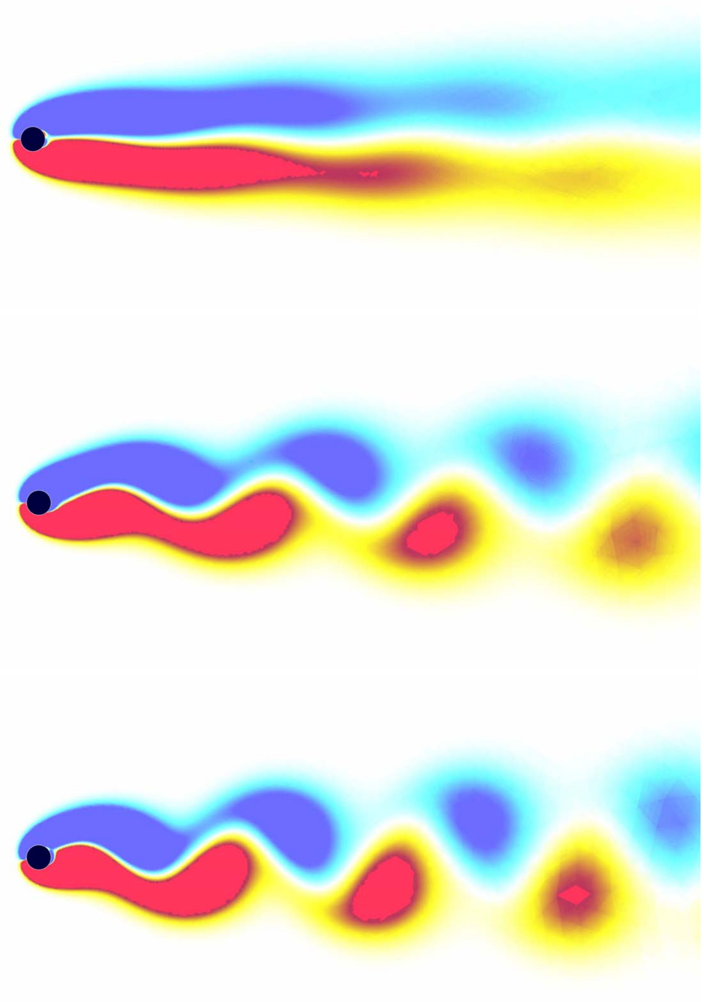

FIGURE 8. Vorticity field at final time, Ur=7.5 and Re=20, 22, 24 from top to bottom.

Fig. 8 shows vorticity fields at final simulation times for Ur=7.5 and Re=20, 22, 24. We observe that at $Re = 20$, the wake doesn't resembles to a vortex street. We could define this configuration as wake-induced vibrations rather than vortex-induced vibrations. For Re =22 and 24, oscillations may be qualified as vortex-induced vibrations. If the vortex formation length is quite large, vorticity cells are well defined in the wake. Fig. 8 shows vorticity fields at higher reduced velocities and for a Reynolds number value of 35. The occurrence of a vortex street evidenced for these two cases. We may infer that most of cases can be qualified as vortex-induced vibrations and that only cases for which the vibration amplitude (A/D) is lower than 0.05 would correspond to wake-induced vibrations.

5 Conclusion

Vortex-induced vibrations of an isolated circular with zero mass and zero structural damping for values of the Reynolds number below the first Hopf bifurcation have been simulated. It has been shown that VIV and wake-induced vibrations for amplitude lower than $0.05D$ are likely to occur for values of the Reynolds number as low as 20. The cylinder undergoes vibrations at least up to values of 40 of the reduced velocity (Ur). Our results follow observations obtained by Mittal *et al.* [3] in the sense that VIV are likely to occur for values as low as 20 when the reduced velocity is near to 7. We did not observe in-line vibrations. As a matter of fact, in-line vibrations are expected for reduced velocities below 3 and we performed simulations for re-

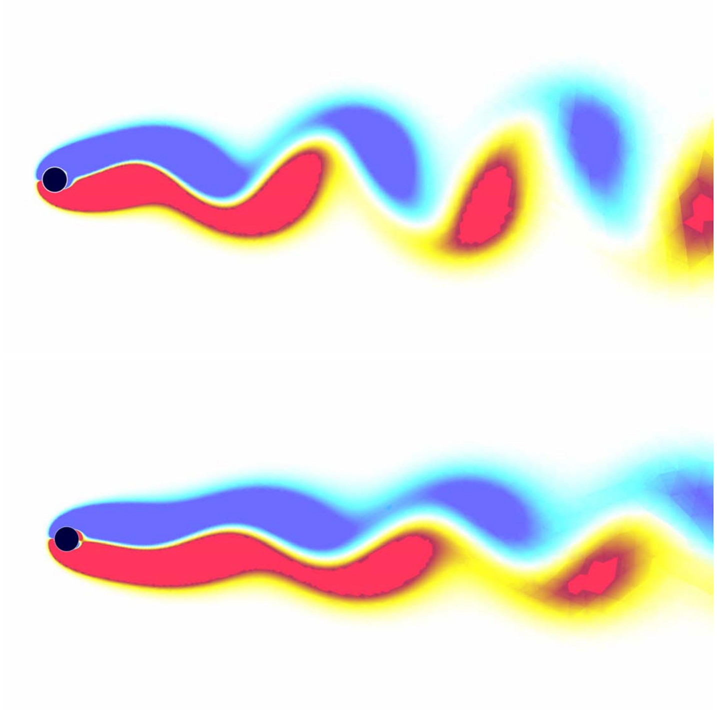

FIGURE 9. Vorticity field at final time, Ur=30, 40 from top to bottom and Re=35.

duced velocities higher or equal to 3.5.

Present results could be improved by increasing the number of simulations in order to better resolve the low Reynolds number limit of vibrations. Also, in Mittal and Singh [3] it is shown that the maximum amplitude of vibration increases with mass ratio. By performing another study with a mass ratio of $m^* = 0.1$, we should be able to determine if the boundary obtained for $m^* = 0$ corresponds to the ultimate boundary of transverse vibrations in the (Re, Ur) plane.

REFERENCES

[1] C.W. Van Atta and M. Gharib. Ordered and chaotic vortex streets behind circular cylinders at low reynolds numbers. *Journal of Fluid Mechanics*, 174:113–133, 1987.

[2] C. Cossu and L. Morino. On the instability of a spring-mounted circular cylinder in a viscous flow at low reynolds numbers. *Journal of Fluids and Structures*, 14:183–196, 2000.

[3] S. Mittal and S. Singh. Vortex-induced vibrations at subcritical re. *Journal of Fluid Mechanics*, 534:185–194, 2005.

[4] B. Stappenbelt and F. Lalji. Vortex-induced vibration super-upper response branch boundaries. *International Journal of Offshore and Polar Engineering*, 18:99–105, 2008.

[5] D. Shiels, A. Leonard, and A. Roshko. Flow-induced vibration of a circular cylinder at limiting structural parameters. *Journal of Fluids and Structures*, 15:3–21, 2001.

[6] H. Schlichting. *Boundary-Layer Theory*. McGraw-Hill, 7th edition, 1979.

[7] M. Lacroix and A. Garon. Numerical solution of phase change problems: an eulerian-lagrangian approach. *Numerical Heat Transfer, Part B*, 19:57–78, 1992.

[8] M. Heil. Stokes flow in an elastic tube - a large-displacement fluid-structure interaction problem. *Journal for Numerical Methods in Fluids*, 28:243–265, 1998.

[9] P. A. Sackinger, P. R. Schunk, and R. R. Rao. A newton-raphson pseudo-solid domain mapping technique for free and moving boundary problems: A finite element implementation. *Journal of Computational Physics*, 125:83–103, 1996.

[10] E. Hairer and G. Wanner. *Solving Ordinary Differential Equations II, Stiff and Differential-Algebraic Problems, 2^{nd} revised edition*. Springer, Germany, 2002.

[11] O. Schenk and K. Gärtner. Solving unsymmetric sparse systems of linear equations with pardiso. *Journal of Future Generation Computer Systems*, 20(3):475–487, 2004.

[12] O. Schenk and K. Gärtner. On fast factorization pivoting methods for symmetric indefinite systems. *Elec. Trans. Numer. Anal.*, 23:158–179, 2006.

[13] S. Etienne, A. Garon, and D. Pelletier. Perspective on the geometric conservation law and finite element methods for ale simulations of incompressible flow. *Journal of Computational Physics*, 228:2313–2333, 2009.

[14] K.H. Halse. *On vortex shedding & predictions of VIV of circular cylinders*. PhD thesis, NTNU Trondheim, 1997.

[15] J.Y. Sa and K.S. Chang. Shedding patterns of the near wake vortices behind a cylinder. *Int. Journal for Numerical Methods in Fluids*, 12:463–474, 1991.

[16] M. Braza. *Etude numérique du décollement instationnaire externe par une formulation vitesse-pression : Application à lécoulement autour dun cylindre circulaire.* PhD thesis, Institut National Polytechnique, Toulouse, 1981.

[17] H. Blackburn, R. Govardhan, and C.H.K. Williamson. A complementary numerical and physical investigation of vortex-induced vibrations. *Journal of Fluids and Structures*, 15:481–488, 2000.

[18] J. Yang, S. Preidikman, and E. Balaras. A strongly coupled, embedded-boundary method for fluid-structure interactions of elastically mounted rigid-bodies. *Journal of Fluids and Structures*, 24:167–182, 2008.

[19] E. Buffoni. Vortex-shedding in subcritical conditions. *Physics of Fluids*, 15:814–816, 2003.